




Reflectance evaluation of eye fundus structures with a visible and near-infrared multispectral camera

FRANCISCO J. BURGOS-FERNÁNDEZ,^{1,*} TOMMASO ALTERINI,¹ 
FERNANDO DÍAZ-DOUTÓN,¹ LAURA GONZÁLEZ,² CARLOS MATEO,²
CLARA MESTRE,³ JAUME PUJOL,¹ AND MERITXELL VILASECA¹

¹Center for Sensors, Instruments and Systems Development, Universitat Politècnica de Catalunya, Rambla Sant Nebridi 10, Terrassa, 08222, Spain

²Instituto de Microcirugía Ocular (Miranza Group), Josep Maria Lladó Street 3, Barcelona, 08035, Spain

³Indiana University School of Optometry, 800 Atwater Ave, Bloomington, IN 47405, USA

*francisco.javier.burgos@upc.edu

Abstract: We examined the spectral reflectance of fundus structures in the visible and near-infrared (400–1300 nm) range for contributing to the medical diagnosis of fundus diseases. Spectral images of healthy eye fundus and other ocular diseases were acquired using a novel multispectral fundus camera. Reflectance metrics were computed based on contrast to analyze the spectral features. Significant differences were observed among the structures in healthy and diseased eye fundus. Specifically, near-infrared analysis allows imaging of deeper layers, such as the choroid, which, to date, has not been retrieved using traditional color fundus cameras. Pathological structures, which were hardly observable in color fundus images owing to metamerism, were also revealed by the developed multispectral fundus camera.

© 2022 Optica Publishing Group under the terms of the [Optica Open Access Publishing Agreement](#)

1. Introduction

The study of the ocular fundus aids in the investigation and earlier diagnosis of many retinal diseases, which lead to changes in the concentration of particular substances and location and thickness of retinal structures, eventually leading to different fundus reflectance values [1]. For instance, an increase in intraocular pressure (IOP) in patients with glaucoma affects the nerve fiber layer (NFL), causing changes in its reflectance that can be detected by fundus imaging [2]. Age-related macular degeneration (ARMD) can be diagnosed by examining the accumulation of drusen and autofluorescent pigments, such as lipofuscin and carotenoids, or by studying the reflectance of melanin [3]. The choroid might be affected in different retinal disorders, such as ARMD, but also in primary conditions, such as choroidal tumors, which are difficult to distinguish via conventional color retinography [4].

The spectral properties of the eye are mainly determined by those of the water, proteins, and chromophores. Wavelengths below 400 nm and above 1400 nm are strongly absorbed by the cornea, aqueous humor, lens, and vitreous. Hence, only wavelengths in the range of 420–920 nm, where the ocular transmittance is higher than 0.4, are available for better detection of the eye fundus [2]. Accordingly, only light within the visible (VIS) and near-infrared (NIR) ranges reaches the retina. The most superficial reflecting structure in the ocular fundus is the inner retinal membrane, which presents flat spectral reflection [5]. The NFL is located immediately after the inner retinal membrane, showing higher reflectance values at 460 nm that decrease towards 560 nm, with just slight changes between 560 nm and 680 nm [6]. The retinal pigment epithelium (RPE) and choroid exhibit high melanin concentration, and they absorb wavelengths especially in the ultraviolet (UV) and blue range. This is further supplemented by the absorption of macular carotenoids (e.g., lutein and zeaxanthin) between 390 nm and 540 nm with a maximum at 460

nm [7]. Lipofuscin is a yellow-brown pigment located at the RPE, and it has A2E as a major fluorophore, with absorbance peaks at 285, 340, and 420 nm, and emission at approximately 600 nm [8,9]. Conversely, hemoglobin can be used for direct measurements of the ocular metabolism. Oxygenated blood shows spectral absorption maxima at 416, 540, and 575 nm and minima at 510 and 560 nm, whereas de-oxygenated blood shows a local minimum at 470 nm and local maximum at approximately 560 nm. Furthermore, in the NIR (around 800 nm), there is a shift in their spectral absorption curves that is used to differentiate between them in pulse oximetry [8,10].

Quantitative assessments of the ocular fundus were initially performed using fundus reflectometry [8], which applies densitometry to conventional ophthalmoscopy and spectrography, to study the visual pigment [11] and oxygen concentration [12]. In the 90s, charge-coupled-device (CCD) cameras were used to obtain quantitative measurements of the integrated reflectance over the entire pupil plane for the first time [13]. Simultaneously, scanning laser ophthalmoscopes (SLOs) were introduced as instruments with enhanced signal-to-noise ratios even though they are more restricted in terms of spectral sampling because they only use a single monochromatic laser as a light source [14].

Recently, multispectral imaging (MSI) has been considered as a technology with significant potential for eye fundus diagnosis because it exhibits a good compromise between spatial and spectral sampling. Nevertheless, most of the MSI devices consist of traditional fundus cameras with the original illumination or detection systems replaced, they have low spatial resolution and require spatial scanning [12], or they exhibit slow spectral sampling owing to the use of interferential [15,16] or tunable filters [17,18]; hence, they were non-optimal solutions. Other studies include broadband light-emitting diodes (LEDs) and narrow-band filters that allow good and faster spectral sampling without compromising spatial resolution [19–21]. The fact that the acquisition time of these devices is above 1 s can lead to artifacts due to eye movements; to avoid this, some of them only include few spectral bands. Snapshot MSI posed a solution to this problem, but at the expense of spatial resolution ($< 350 \times 350$ pixels) and computational cost [22–24].

Additionally, most of these systems operate in the VIS range, and just a few perform in the NIR, mainly below 900 nm [16,21,25,26]. Some works proposed approaches exploring longer wavelengths, such as 940 nm [27] or 970 nm [28], but none of them reported bands beyond 1000 nm. However, this range can provide useful information from often hidden fundus layers, such as the RPE and choroid, as light penetrates deeper into the tissue at these wavelengths.

Therefore, in this study, we aimed to evaluate the spectral reflectance of fundus structures in healthy and pathological eye fundus using a novel customized multispectral fundus camera that overcomes all the limitations described. This device is based on narrow-band LEDs, which performs fast imaging of the eye fundus in the VIS and NIR regions (400–1300 nm) with high spectral (15 bands) and spatial resolution [29]. The system is sensitive in the relatively unexplored range beyond 900 nm, the so-called second NIR window [30], which can potentially be useful for improving the medical diagnosis of certain ocular diseases, especially those affecting the deeper fundus layers.

2. Materials and methods

2.1. Patients

In this prospective, observational, cross-sectional, non-consecutive case series study, we analyzed eyes from two adult population groups: healthy patients (control group) and patients with ocular diseases exhibiting abnormal fundus structures (diseased group). Trials were conducted from March 2019 to December 2020 at the Instituto de Microcirugía Ocular (IMO-Miranza Group, Barcelona, Spain) and Vision University Centre (CUV) of the Universitat Politècnica de Catalunya (Terrassa, Spain) under the supervision of an ophthalmologist (C. M.). The Declaration of Helsinki tenets of 1975 (revised in Tokyo in 2004) were followed throughout the study. Ethical

committee approval was obtained and all patients provided written informed consent before undergoing any examination.

Table 1 shows patient demographics, number of eyes, average subjective refraction, and best-corrected visual acuity (BCVA). The inclusion criteria were as follows: subjective spherical refraction between $\pm 15D$ and astigmatism $\leq 2D$ (spherical refraction limited by the multispectral fundus camera correction range and low astigmatism to obtain acceptable images without high distortion); for subjects belonging to the control group, BCVA equal to or higher than 0.9 in decimal units (20/22.2 Snellen), intraocular pressure (IOP) ≤ 21 mmHg, normal fundus, and no history of any other ocular condition or trauma; for patients in the diseased group, any pathology affecting the eye fundus, such as glaucoma and ARMD, among others. The exclusion criteria included the diagnosis of any other ocular or systemic disease affecting the eye differently when compared to the previous diseases, especially those that alter the transparency of the ocular media. Nevertheless, healthy eyes or eyes with a retinal disease, which had undergone cataract surgery with implantation of an intraocular lens (IOL), were included in the study.

Table 1. Patient demographics, subjective refraction (sphere, cylinder), and BCVA of the control and diseased groups (mean \pm SD [range]).

	Control group	Diseased group
Number of patients	137 (8 with IOL)	30 (17 with IOL)
Number of eyes	245 (10 with IOL)	60 (22 with IOL)
Gender (%)	87 F (64%); 50 M (36%)	21 F (70%); 9 M (30%)
Age (years)	41.01 \pm 16.88 [19, 80]	67.60 \pm 15.30 [19, 91]
Sphere (D)	-0.45 \pm 2.11 [-8.00, 8.00]	0.04 \pm 2.44 [-10.50, 4.50]
Cylinder (D)	-0.74 \pm 0.64 [-2.00, 0.00]	-0.87 \pm 0.70 [-2.00, 0.00]
BCVA	1.02 \pm 0.16 [0.9, 1.5]	0.64 \pm 0.30 [0.01, 1.00]

A total of 506 eyes of 253 patients were included in the study. A total of 306 eyes (153 patients) were included in the control group and 200 eyes (100 patients) were included in the diseased group. The advanced age and visual impairment caused fixation problems to some patients, leading to artifacts in the images that cannot be removed; owing to this, 201 eyes were finally excluded with a final count of 245 healthy and 60 diseased eyes.

2.2. Instruments and procedures

In addition to regular ophthalmic and optometric examinations including tonometry, slit-lamp biomicroscopy, retinoscopy, and manifest subjective refraction, participants underwent conventional color retinography and optical coherence tomography (OCT). Images were acquired using a mydriatic color fundus camera TRC-50DX (Topcon Corp., Itabashi, Japan) and CIRRUS HD-OCT (Carl Zeiss AG, Oberkochen, Germany) at IMO. Furthermore, when the patient's pupil was not dilated, images were acquired using an Optomap fundus camera (Optos Inc., Dunfermline, United Kingdom). At CUV, the 3D OCT-1 Maestro (Topcon Corp., Itabashi, Japan) was used to obtain OCT records and acquire color fundus images.

Moreover, fundus images were acquired with a customized non-mydriatic multispectral fundus camera [29], which consists of two detection arms, one for the spectral range from 400 nm to 950 nm (VIS–NIR detection arm; CMOS camera: 2048 \times 2048 pixels, pixel size 6.5 μ m, and 16-bit depth) and another for the range from 960 nm to 1300 nm (NIR detection arm; InGaAs camera: 640 \times 512 pixels, pixel size 20 μ m, and 14-bit depth). It also includes a LED-based illumination system with 15 spectral bands, with peak wavelengths of 416, 450, 471, 494, 524, 595, 598, 624, 660, 732, 865, 955, 1025, 1096, and 1213 nm. The exposure time was set to 11 ms for the VIS–NIR bands (416–955 nm) and to 100, 120, and 100 ms for the other NIR bands

(1025, 1096, and 1223 nm). The complete acquisition lasts 612 ms (264 ms for the VIS-NIR arm and 348 ms for the NIR arm), synchronizing the LEDs emission and the cameras shuttering through signal triggering. This fast measurement is one of the main advantages of this prototype, and so patient's discomfort is minimized and artifacts due to eye movements are avoided. This acquisition time approaches those of snapshot multispectral systems; in fact, the required time is even much below most multispectral systems with sequential acquisition (requiring times above 1-3 s while evaluating less bands) [16,17,25,28]. The fundus camera features an angular field of view (FOV) of 30° and allows compensating patient's spherical refraction up to ± 15 D.

2.3. Image processing and spectral reflectance retrieval

Once the raw spectral images were acquired, they were first processed (e.g., dark-image subtraction and shadow correction) to obtain reflectance data that were free from artifacts (mainly due to back-reflections and non-uniformities of the illumination on the fundus). Then, reflectance was computed at each wavelength as shown in Eq. (1) to compensate for the spectral response of the system, which differs in each spectral band owing to differences in the quantum efficiency (QE) of the cameras and radiant power of the LEDs that are included.

$$R(\lambda) = R_W(\lambda) \frac{I(\lambda)}{I_W(\lambda)} \quad (1)$$

Specifically, $R(\lambda)$, $I(\lambda)$, and $I_W(\lambda)$ denote the reflectance image, raw image, and image of a calibrated reference white (BN-R98-SQC, Gigahertz-Optik GmbH, Germany), respectively; the calibration of the reference white is included in $R_W(\lambda)$. The formula applies for each pixel (i, j) in the images.

For each structure, its reflectance was then assessed by computing the mean value over the pixels of three different regions of interest (ROIs) with a predefined size depending on the structure type: nerve fibers = 0.01°, retinal and choroidal vessels = 0.1°, optic disc and fundus without structures = 0.2°, and fovea = 0.4°. Because of the large variability among pathological structures, the ROIs were adjusted between 0.01° and 0.4° to ensure the retrieval of meaningful spectral information. In each case, the center of the ROI was manually selected.

Given that the light coming from the ocular fundus is affected by the transmittance of the preceding ocular media, which might differ slightly for each patient even in the absence of pathologies and also due to small misalignments between the eye and camera, absolute comparisons in terms of reflectance among subjects can potentially lead to some discrepancies. To mitigate this, a contrast parameter, termed as global contrast (GC; Eq. (2)), was calculated by dividing the reflectance of any ocular structure under study, $R(\lambda)$, by the mean reflectance value obtained by averaging the entire fundus image, i.e., the entire FOV of the camera, $R_{FOV}(\lambda)$. A more local quantification, termed as local contrast (LC; Eq. (3)), was additionally used to compare data extracted from two close areas, x and y , by computing the ratio between their reflectance values, $R_x(\lambda)$ and $R_y(\lambda)$, respectively. This evaluation, in which residual illumination inhomogeneities are even more minimized than those in the GC analysis, can be particularly helpful when small lesions, such as RPE alterations and healthy surrounding tissues are compared. Figure 1 exemplifies the used ROIs for GC (Fig. 1(A)) and LC (Fig. 1(B)) computations. A self-standing software application developed in MATLAB R2018b (The MathWorks, Inc., Natick, United States) was implemented to perform the aforementioned computational procedures.

$$GC(\lambda) = \frac{R(\lambda)}{R_{FOV}(\lambda)} \quad (2)$$

$$LC(\lambda) = \frac{R_x(\lambda)}{R_y(\lambda)} \quad (3)$$

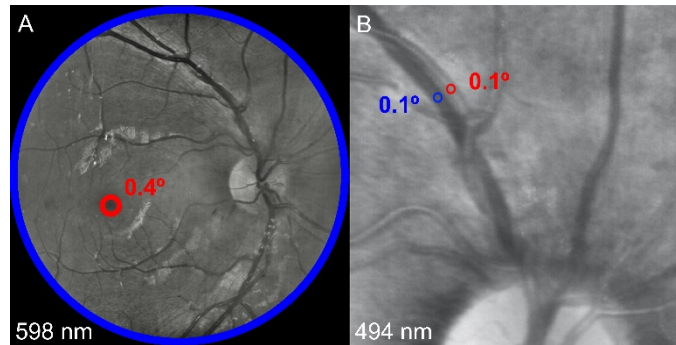


Fig. 1. (A) Spectral image depicting the ROI used for the computation of the GC of the fovea (red circle) and the entire FOV (blue circle). (B) Spectral image depicting two of the ROIs used for the computation of the LC between arteries (red circle) and veins (blue circle).

3. Results and discussion

3.1. Control group

Figure 2 shows 15 spectral images acquired using the multispectral fundus camera for a healthy eye. The images acquired beyond 900 nm, which have been relatively unexplored with traditional retinography or former spectral imaging systems adapted for fundus photography, revealed deep layers and vasculature, especially the choroid. When compared to previous systems, the system used in this study includes more spectral bands with a higher spatial resolution [29]. Furthermore, the system expands the spectral sensitivity in the NIR range. Acquisition of images beyond 1300 nm was not possible due to water absorption in the preceding ocular media and low QE of the InGaAs camera. Additionally, the image at 416 nm was of poor quality because of the strong lens absorption at UV wavelengths.

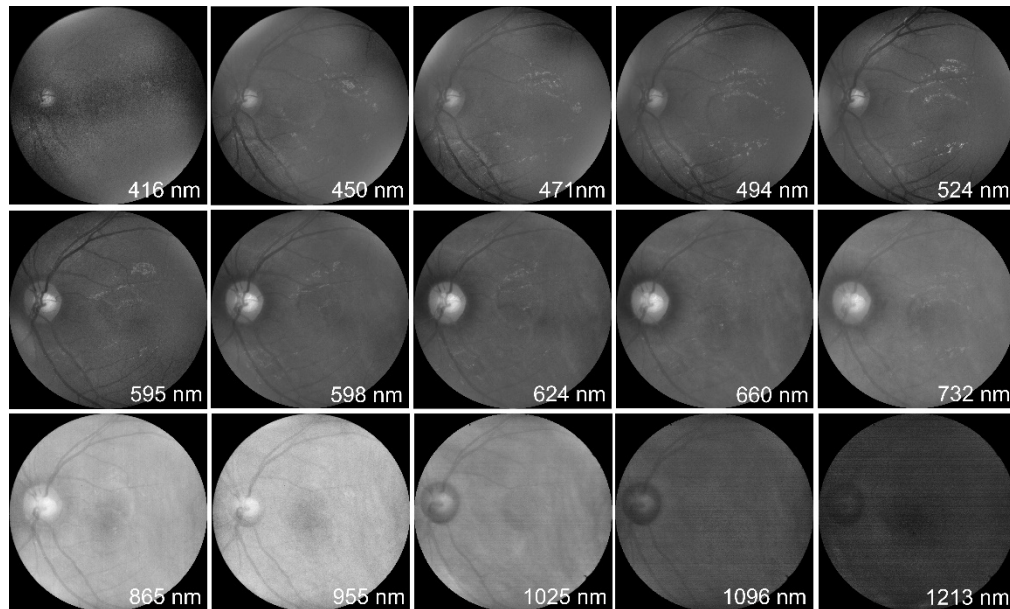


Fig. 2. Complete sequence of spectral images of a healthy eye acquired with the multispectral fundus camera.

The mean spectral curves of several fundus structures, considering that all healthy eyes are analyzed in terms of reflectance, are depicted in Fig. 3. Although no significant differences were observed as a function of age, patients undergoing cataract surgery with an implanted IOL (all of them ≥ 70 years old) showed absolute reflectance values that were significantly higher than the rest (dashed lines in Fig. 3) except below 550 nm, where lower values were observed due to the stronger UV-blue protection offered by IOLs. With the exception of the optic disk, only subtle differences among structures can be observed in terms of reflectance as they are not only influenced by the reflectance of the retina itself, but also by transmission through the preceding ocular media. Hence, the dominance of water-like absorbance in the reflectance curves is evident as previously reported by other authors [2,8]. Fundus reflectance was observed to gradually increase with wavelength in the VIS range (as absorption of hemoglobin and melanin becomes lower). The maximum value of fundus reflectance is observed at 850 nm, and then, it starts decreasing as the water absorbance increases. Specifically, the valley at 1025 nm coincides with a water absorption peak, whereas the local maximum recorded at 1096 nm corresponds to a lower water absorbance (between 1000 and 1150 nm). Nevertheless, analysis with GC values allows us to eliminate the influence of ocular transmission, and thereby, making it easier to identify individual spectral signatures of different structures.

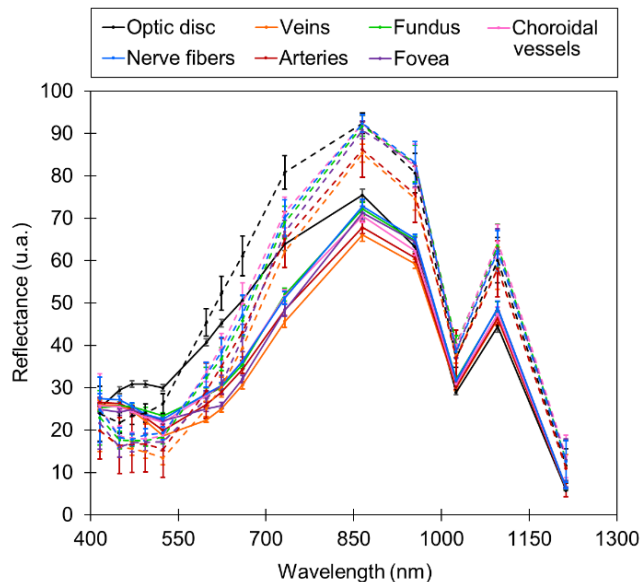


Fig. 3. Mean \pm standard error of the reflectance (Eq. (1)) for different healthy eye fundus structures. Solid lines denote patients below 70 years while dashed lines denote patients above 70 years (all of them with IOL). The reflectance from the fundus refers to reflectance of those regions where neither retinal structures, such as arteries, veins, and fovea, nor choroidal vessels are present.

A detailed analysis of the fundus structures was conducted for specific cases. Specifically, nerve fibers can be clearly observed as whitish threads in spectral images, travelling towards the optic disk along with the retinal vessels (Fig. 4). Conversely, in the RGB image, they are hardly recognizable. Several authors have proven that NFL is especially visible in red-free images, with maximum reflectance at the blue-green part of the spectrum, particularly below 560 nm [6,10,31]. A similar behavior is observed in terms of GC (Fig. 4(B)) for which maximum values are reached below 500 nm and decrease towards 550 nm with a very flat spectra along the rest of the spectral range [6]. This increased reflectance at short wavelengths is due to the fact that nerve

fibers are superficially located in the retina in addition to their chemical composition. Hence, it should be noted that unlike confocal SLOs, light coming from different depths is simultaneously recorded in MSI systems. In this case, the LC curve is similar to the GC curve of nerve fibers (dashed black and solid red curves in Fig. 4(B), respectively) because the surrounding tissue and the mean reflectance of the entire fundus are similar. Furthermore, this leads to the similarity between the LC and GC for other structures as shown in the subsequent figures. The optic disk is visible from 400 nm to 1000 nm (Fig. 2) because nerve fibers are covered by myelin and merge with collagen fibers as a multilayer network structure when leaving the eye through the optic disk as a dense and thick bundle. This leads to the formation of the lamina cribrosa, which has high reflectivity in this range [6]. Furthermore, this is due to the absence of other retinal layers, which prevent higher absorption [32], particularly at the center of the optic disk.

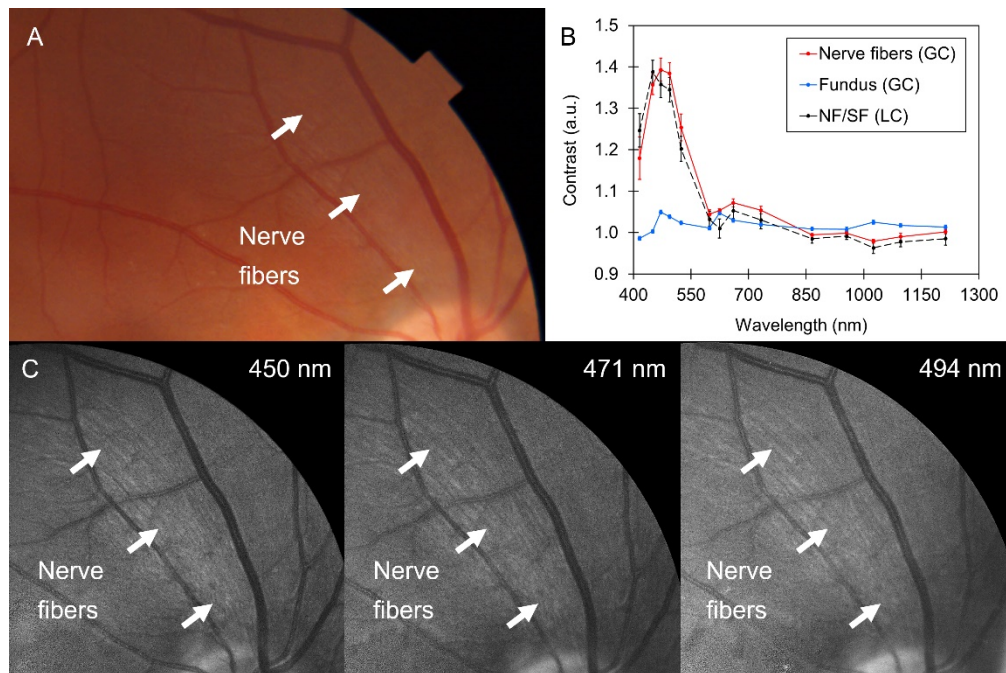


Fig. 4. (A) RGB fundus image, (B) mean \pm standard error of the global contrast (GC) and local contrast (LC) (Nerve Fibers, NF/Surrounding Fundus, SF) and (C) spectral images showing nerve fibers. The statistics plotted in (B) consider the spectral reflectance of different regions within this eye, which was specifically selected to show this fundus structure. The plots contained in the following figures are also based on the evaluation of different regions of one single eye fundus.

The spectral images of the arteries and veins are shown in Fig. 5. The different absorption features of oxygenated and deoxygenated blood are evident in terms of GC and LC as well as in the images. Arteries are brighter than veins (and also linked to larger GC values), especially between 524 nm and 732 nm, because of the lower absorption of oxygenated blood in this range [8,33]. They exhibit a similar appearance for shorter and longer wavelengths. The lowest reflectance for arteries and veins, in accordance with previous studies [8,10,22], was recorded for wavelengths between 525 and 600 nm, where absorption peaks of hemoglobin have been reported. In conventional retinography, the wavelength range below 600 nm corresponds to the range where red-free images are usually acquired because the contrast of retinal vessels is maximized with

respect to the surrounding tissue owing to the higher absorption of oxygenated and deoxygenated hemoglobin. However, it is difficult to differentiate between veins and arteries in this range.

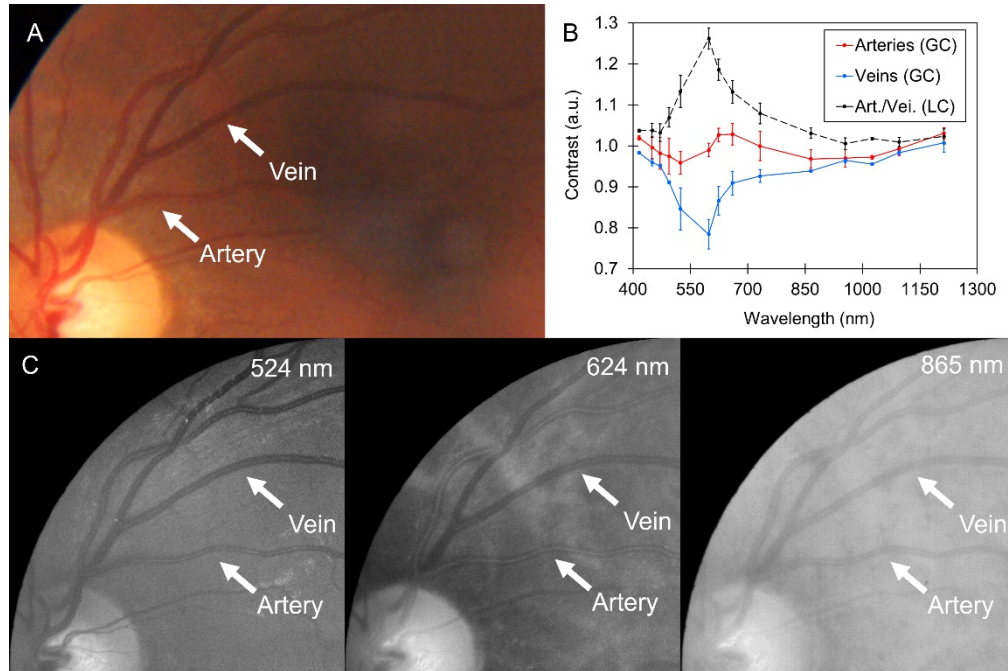


Fig. 5. (A) RGB fundus image, (B) mean \pm standard error of the global contrast (GC) and local contrast (LC) (Arteries, Art./Veins, Vein.), and (C) spectral images showing arteries and veins.

In pulse oximetry [34], differences in the absorption of oxyhemoglobin and deoxyhemoglobin within the spectral range of 700–900 nm are traditionally used to measure oxygen saturation. Some attempts have been made to use fundus imaging for the characterization of retinal metabolism using VIS wavelengths (between 520 and 600 nm). Nevertheless, a thorough preliminary calibration must be conducted to account for scattering and absorption effects and variation in melanin pigment [35–37]. For example, a precise fit to a linear combination of reference curves obtained from fully saturated and desaturated red cell suspensions has been used [22]. The spectral information measured with the developed fundus camera beyond 700 nm can be extremely valuable for mimicking traditional pulse oximetry in terms of wavelengths, and thereby, improving the accuracy of oxygen saturation measurements using fundus imaging. Additionally, the use of this spectral range can be advantageous because glare, which is present in the VIS range, does not affect patients' comfort, leading to a more dynamic measurement.

The fovea can be clearly identified in spectral images acquired at short wavelengths (Fig. 6) as it acts as a blue filter (with a sharp valley around 450 nm in terms of GC) because of the presence of macular carotenoids with strong absorption between 460 nm and 480 nm [7–8]. The enhanced contrast at blue wavelengths no longer exists beyond 524 nm (Fig. 6(C)). Given that the tissue surrounding the fovea exhibits spectral reflectance features that are highly similar to those obtained when averaging the entire FOV (as performed in the GC), the GC curve for the fovea and LC are very similar in this case. Although lipofuscin (A2E fluorophore) is distributed throughout the RPE, it can contribute to the absorption peak at 450 nm because the RPE is more exposed in the fovea [8,9]. Additionally, the foveal capillaries can partially explain the reduced reflectance between 500 and 600 nm because the absorbance of hemoglobin is maximal here.

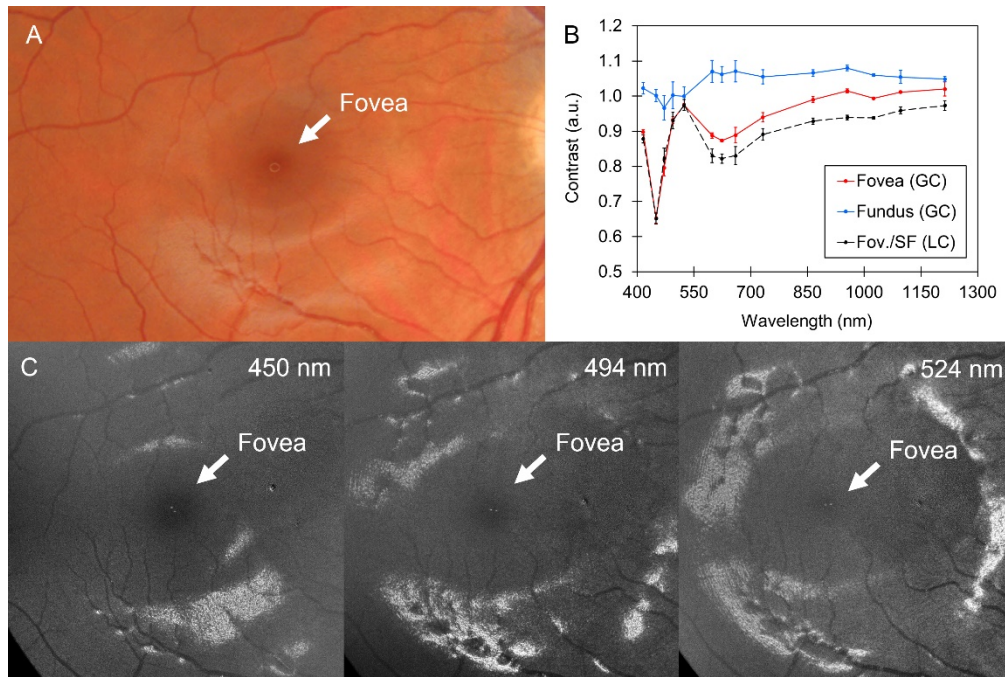


Fig. 6. (A) RGB fundus image, (B) mean \pm standard error of the global contrast (GC) and local contrast (LC) (Fovea, Fov./Surrounding Fundus, SF), and (C) spectral images showing the fovea.

Choroidal layers cannot be observed at shorter wavelengths because of the strong absorption of melanin, which decreases beyond 595 nm and allows light to penetrate at a deeper level [8]. Therefore, choroidal vessels can be distinguished beyond this wavelength. Figure 7 shows that choroidal vessels exhibit a slightly higher reflectance when compared to the overall fundus between 595 nm and 732 nm (positive contrast), whereas a contrast shift is recorded at wavelengths exceeding 865 nm (see Fig. 7(C)). The GC values obtained for choroidal vessels correlated with those reported in previous studies, which relate their absorption spectrum to that of oxyhemoglobin [10]. Additionally, they appear darker in the NIR region because light penetrates deeper inside the tissue and is reflected back at the sclera (Fig. 7(C) at 1025 nm and 1096 nm). Therefore, choroidal vessels shade a portion of the reflected light. Hence, NIR imaging can be used to diagnose disorders that can affect the deep layers of the fundus such as the choroid.

3.2. Diseased group

Figure 8 shows fundus images and spectral curves from a retina with hard and soft drusen, the last being the first signs of ARMD. In RGB images, drusen are less distinguishable because of metamerism, whereas they can be better observed in spectral images acquired at specific wavelengths. Soft drusen were linked to higher values of GC (Fig. 8(B)) at wavelengths shorter than 600 nm. At longer wavelengths, the contrast switches and hard drusen become more reflective (see Figs. 7(C) and 7(D)). This is highlighted in terms of LC, which corresponds to the ratio between the hard and soft drusen reflectance values.

The drusen location (depth) is not considered to influence their spectral properties because it is rather specific. They are placed at Bruch's membrane. The evaluated soft and hard drusen exhibited reflectance peaks in the range of 500–600 nm as reported in the literature [23]. The

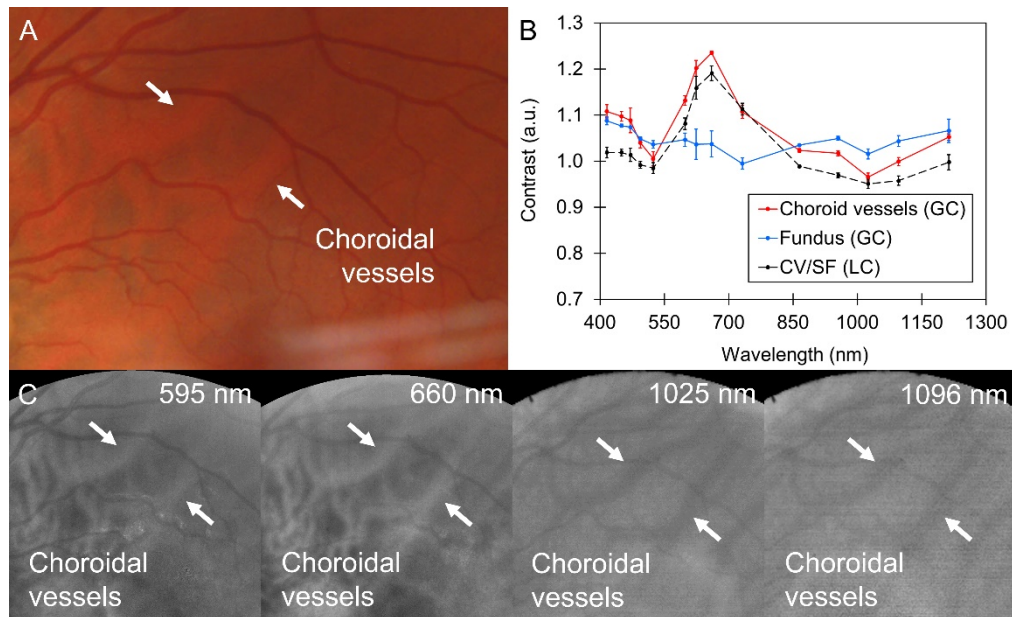


Fig. 7. (A) RGB fundus image, (B) mean \pm standard error of the global contrast (GC) and local contrast (LC) (Choroidal Vessels, CV/Surrounding Fundus, SF) and (C) spectral images showing choroidal vessels.

higher reflectance of soft drusen at short wavelengths can be due to the autofluorescent emission of substances, such as lipofuscin, which is relevant up to 600 nm [8,9]. Conversely, hard drusen show a higher reflectance at longer wavelengths probably because they are usually associated with RPE degeneration and depigmentation.

Advanced stage ARMD can lead to signs other than drusen such as scars and hemorrhages. In the RGB image shown in Fig. 9, the macular scar appears as a black, poorly demarcated region, whereas the spectral images and curves reveal a strong absorption between 500 nm and 950 nm. As reported in a previous study, this is due to the composition of the lesion consisting of coagulated blood (absorption below 600 nm) and fibrotic tissue (absorption below 1000 nm) [38]. Scars are still visible at red and NIR wavelengths because they are typically located at the interface between the retina and choroid, i.e., deeper than other fundus structures. The hemorrhage near the scar also absorbs light from 500 nm to 950 nm, but to a lesser extent. It gradually disappears towards the NIR region because it is still fluidic (non-oxygenated blood) and does not exhibit a compact fibrotic structure such as scars. Hence, the degree of absorption in the NIR for this type of lesion can be considered an important biomarker for evaluating the progression of degeneration and promptly intervening to reduce the risk of scar formation. Additionally, the contrast at the longest NIR wavelengths (1000–1300 nm) becomes a good indicator of the actual depth of the lesions. For instance, the decrease in contrast in the scar depicted in Fig. 9(B) suggests that the lesion has not significantly extended towards the choroid, but it is just affecting retinal tissue. However, the scar and RPE degeneration shown in Fig. 9(E) are still highly contrasted at 1096 nm, indicating the deeper location in this case.

Conversely, at the early stages of a disease, the detection of any alteration is more difficult and critical because the earlier it is treated, the less damage it causes. Figure 10 depicts the records of an eye with subtle drusen-induced RPE degeneration, which is hardly observable in the RGB image (arrow in Fig. 10(A)), whereas in the spectral images it appears with enhanced contrast. As mentioned above, this is mainly due to the intrinsic metamerism of RGB images, which is

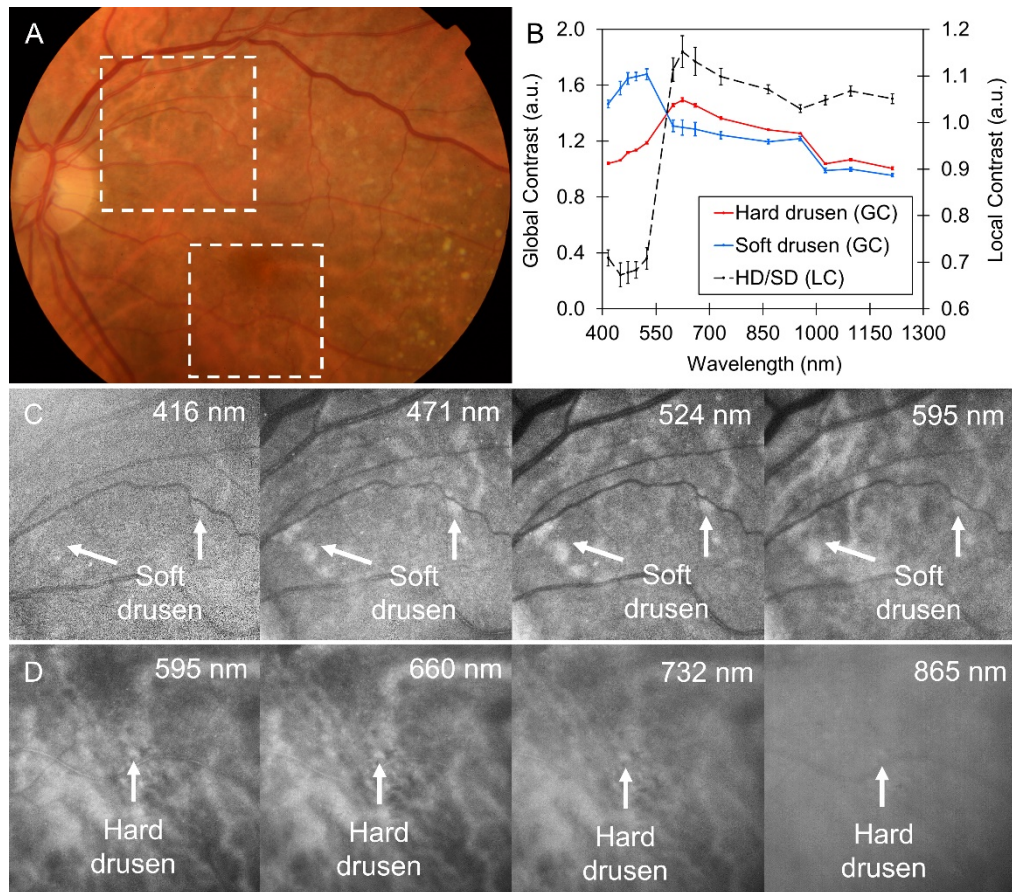


Fig. 8. Eye with drusen. (A) RGB fundus image, (B) mean \pm standard error of the global contrast (GC) and local contrast (LC) (Hard Drusen, HD)/Soft Drusen, SD) and spectral images showing regions with (C) soft and (D) hard drusen.

overcome in spectral analysis. When comparing the GC (Fig. 10(C)) of the fundus (without structures) and that of the RPE degeneration, the latter showed higher values approximately from 500 nm to 1000 nm. The LC follows a similar pattern. Specifically, it is above one even at the longest NIR wavelengths owing to the deep location of the lesion.

In contrast, glaucoma mainly affects the optic disc by altering the relationship between the size of its central and peripheral regions. A common approach involves quantifying the morphological changes by the cup-to-disk ratio using OCT. However, the spectral analysis performed on an eye with glaucoma (Fig. 11) showed that changes can be translated into reflectance values. The LC values, when dividing the reflectance of the center and periphery of the optic disc, were determined as higher, particularly at wavelengths below 700 nm, for glaucomatous eyes when compared to those for healthy eyes. This indicated that the diseased eyes are linked to a higher intensity of the center (Fig. 11(C)) as reported in previous studies [39].

A hypothesis for the increased reflectance at the center of the optic disc in eyes with glaucoma can correspond to the higher exposure of the lamina cribrosa due to enlargement of the optic disc cup. It is likely that light at shorter wavelengths (more influenced by scattering and absorption at the first retinal layers) experiences less scattering and absorption. Hence, the GC and LC differences are higher in this spectral region when comparing healthy and glaucomatous eyes.

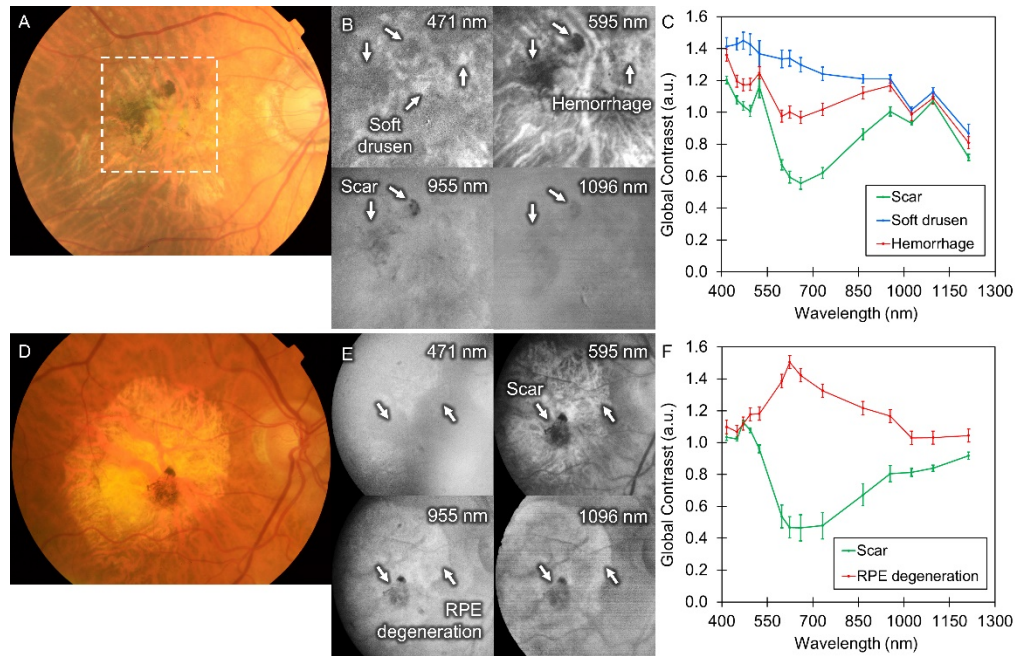


Fig. 9. Two eyes suffering from exudative ARMD. (A, D) RGB fundus images, spectral images showing a region with (B) soft drusen, a scar and hemorrhage, and with (E) an RPE degeneration and a scar, and (C, F) mean \pm standard error of the global contrast (GC) for these structures.

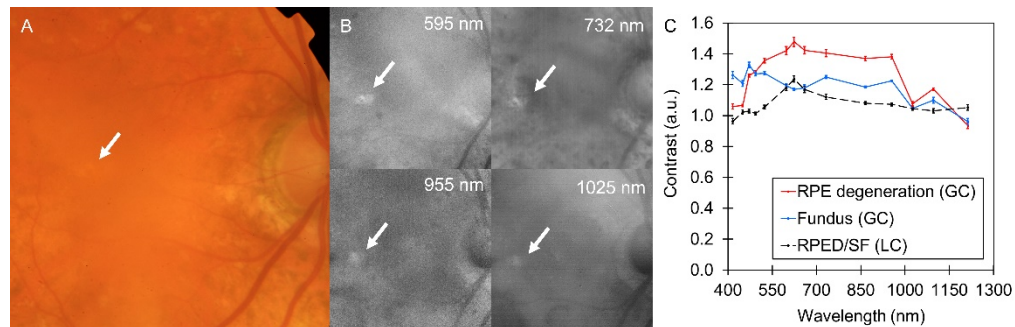


Fig. 10. Eye suffering from a dry ARMD. (A) RGB fundus image, (B) spectral images showing the RPE degeneration, and (C) mean \pm standard error of the global contrast (GC) and local contrast (LC) (RPE degeneration, RPED/Surrounding Fundus, SF).

Owing to the enhanced penetration of longer wavelengths, segmentation of the damaged portion and cup-to-disk assessment can be performed more precisely in NIR images obtained with the developed multispectral fundus camera.

In the eye fundus, other anomalous structures can be observed, representing no risk of disease, such as choroidal nevi, which rarely evolve into malignant melanomas. They are flat, benign areas in the choroid due to the accumulation of pigmented cells. The nevus in Fig. 12 shows good contrast at red-NIR wavelengths (600–1000 nm), where it has a low reflectance. For wavelengths beyond 1000 nm, there is a reflectance shift and it becomes brighter and similar to that of the fundus (Fig. 12(B)). As nevi are located beyond the retina, they exhibit the highest reflectance at

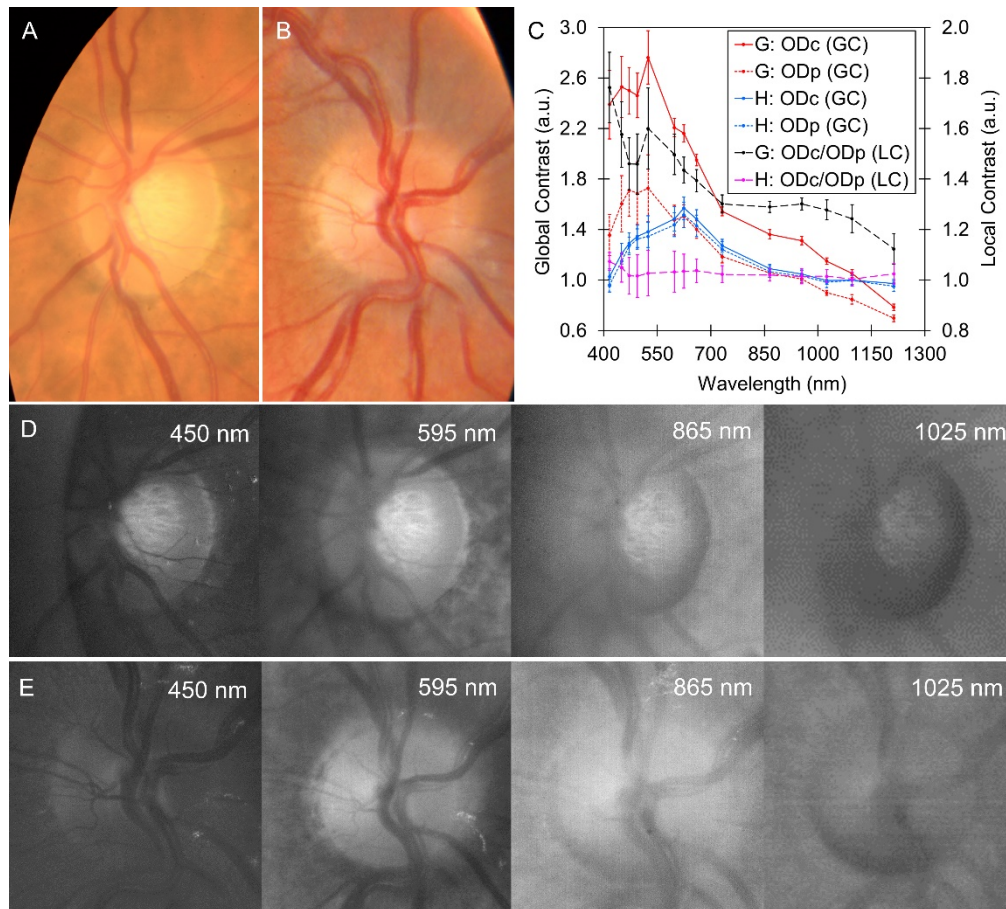


Fig. 11. RGB fundus images of (A) a glaucomatous and (B) healthy eye, (C) mean \pm standard error of the global contrast (GC) of a glaucomatous (G) and healthy (H) eye of the optic disk at the center (ODc) and at periphery (ODp), and local contrast (LC) (ODc/ODp) for both eyes, and spectral images showing the optic disk for (D) a glaucomatous and (E) healthy eye.

longer wavelengths (1000–1300 nm). The data acquired below 624 nm are not relevant because these wavelengths do not penetrate deep into the tissue.

It should be noted that the contrast transition of the nevus analyzed from dark to bright between 955 nm and 1025 nm can be related to the etiology and state of the nevus as well as the state of the RPE tissue in its near surroundings. Hence, some authors concluded that pigmented choroidal nevi surrounded by a halo or circular band of depigmentation exhibits a low probability of turning into melanoma, while nevi without halo can reach a value of 7% [40]. Therefore, the use of spectral information can potentially aid in distinguishing between benign and malignant nevi owing to the increased information on the pigmentation state of the nevus in addition to morphological information provided by OCT records [4,41].

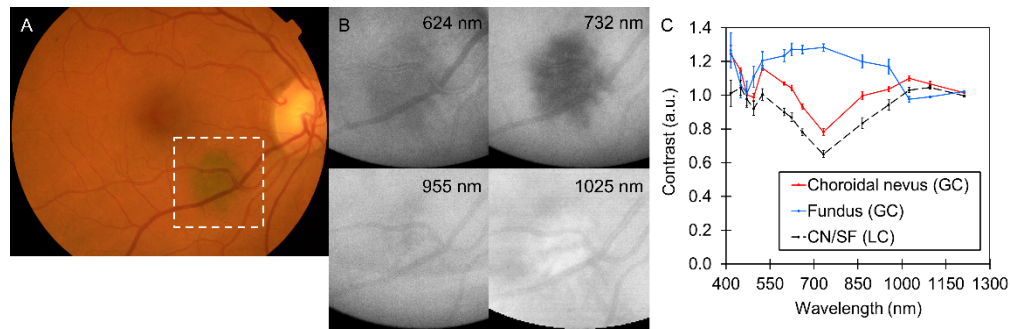


Fig. 12. Eye fundus with a choroidal nevus. (A) RGB fundus image, (B) spectral images, and (C) mean \pm standard error of the global contrast (GC) and local contrast (LC) (Choroidal Nevus, CN/Surrounding Fundus, SF) curves for this structure.

4. Conclusions

The spectral and spatial information obtained with the multispectral fundus camera further advances the qualitative and quantitative interpretation of fundus images and can aid in the diagnosis of retinal diseases. Conversely, it avoids the metamerism of color cameras, and thereby, enhances the visualization of particular structures that usually remain unnoticed. Furthermore, the increased sensitivity in the NIR region is particularly promising because it allows the evaluation of deeper layers and structures, such as lesions affecting the RPE and the choroid, which can be ignored in traditional retinography and can be relevant for early diagnosis of fundus diseases.

Disclaimer

The authors declare that they have no conflicts of interest. This work only expresses the opinion of the authors and neither the European Union nor ACCIÓ are liable for the use made of the information provided.

Funding. H2020 Marie Skłodowska-Curie Actions (801342, Tecniospring INDUSTRY); Agència per a la Competitivitat de l'Empresa (801342, Tecniospring INDUSTRY); Generalitat de Catalunya (801342, Tecniospring INDUSTRY); Ministerio de Ciencia e Innovación - Agencia Estatal de Investigación (MCIN/AEI/10.13039/501100011033, PID2020-112527RB-I00).

Disclosures. The authors declare that there are no conflicts of interest related to this article.

Data availability. Data underlying the results presented in this paper are not publicly available at this time but may be obtained from the authors upon reasonable request.

References

1. C. Regillo, T. Chang, and M. Johnson, "Retina and vitreous," in *Basic and Clinical Science Course* (American Academy of Ophthalmology, 2011).
2. M. Kaschke, K. H. Donnerhacke, and M. S. Rill, *Optical Devices in Ophthalmology and Optometry: Technology, Design Principles and Clinical Applications*, 1st ed. (WILEY- VCH Verlag GmbH, 2014).
3. T. J. Bennett and C. J. Barry, "Ophthalmic imaging today: An ophthalmic photographer's viewpoint - A review," *Clin. Exp. Ophthalmol.* **37**(1), 2–13 (2009).
4. V. L. L. Torres, N. Brugnoli, P. K. Kaiser, and A. D. Singh, "Optical coherence tomography enhanced depth imaging of choroidal tumors," *Am. J. Ophthalmol.* **151**(4), 586–593.e2 (2011).
5. J. M. Gorrard, "Separation of the reflection by the inner limiting membrane," *Ophthalmic Physiol. Opt.* **6**(2), 187–196 (1986).
6. R. W. Knighton, S. G. Jacobson, and C. M. Kemp, "The spectral reflectance of the nerve fiber layer in macaque retina," *Invest. Ophthalm. Vis. Sci.* **30**(11), 2393–2402 (1989).
7. R. A. Bone, J. T. Landrum, L. H. Guerra, and C. A. Ruiz, "Lutein and zeaxanthin dietary supplements raise macular pigment density and serum concentrations of these carotenoids in humans," *J. Nutr.* **133**(4), 992–998 (2003).
8. T. J. M. Berendschot, P. J. DeLintb, and D. V. Norren, "Fundus reflectance—historical and present ideas," *Prog. Retin. Eye Res.* **22**(2), 171–200 (2003).

9. J. R. Sparrow and M. Boulton, "RPE lipofuscin and its role in retinal pathobiology," *Exp. Eye Res.* **80**(5), 595–606 (2005).
10. F. C. Delori and K. P. Pflibsen, "Spectral reflectance of the human ocular fundus," *Appl. Opt.* **28**(6), 1061–1077 (1989).
11. R. A. Weale, "Observations on photochemical reactions in living eyes," *Brit. J. Ophthalmol.* **41**(8), 461–474 (1957).
12. C. Riva, "New ocular fundus reflectometer," *Appl. Opt.* **11**(8), 1845–1849 (1972).
13. S. A. Burns, S. Wu, F. C. Delori, and A. E. Elsner, "Direct measurement of human-cone–photoreceptor alignment," *J. Opt. Soc. Am. A* **12**(10), 2329–2338 (1995).
14. D. van Norren, "Towards improved instrumentation for retinal densitometry," in *Research in Retinitis Pigmentosa. Advances in the Bioscience* (Pergamon, 1987), pp. 177–178.
15. P. Fält, J. Hiltunen, M. Hauta-Kasari, I. Sorri, V. Kalesnykiene, J. Pietilä, and H. Uusitalo, "Spectral imaging of the human retina and computationally determined optimal illuminants for diabetic retinopathy lesion detection," *J. Imaging Sci. Technol.* **55**(3), 30509-1–30509-10 (2011).
16. E. R. de Carvalho, R. J. Hoveling, C. J. van Noorden, R. O. Schlingemann, and M. C. Aalders, "Functional imaging of the ocular fundus using an 8-band retinal multispectral imaging system," *Instrum.* **4**(2), 12 (2020).
17. V. Nourrit, J. Denniss, M. M. K. Muqit, I. Schiessl, C. Fenerty, P. E. Stanga, and D. B. Henson, "High-resolution hyperspectral imaging of the retina with a modified fundus camera," *J. Fr. Ophthalmol.* **33**(10), 686–692 (2010).
18. D. J. Mordant, I. Al-Abboud, G. Muyo, A. Gorman, A. Sallam, P. Ritchie, A. R. Harvey, and A. I. McNaught, "Spectral imaging of the retina," *Eye* **25**(3), 309–320 (2011).
19. N. L. Everdell, I. B. Styles, A. Calcagni, J. Gibson, J. Hebden, and E. Claridge, "Multispectral imaging of the ocular fundus using light emitting diode illumination," *Rev. Sci. Instrum.* **81**(9), 093706 (2010).
20. S. Li, L. Huang, Y. Bai, Y. Cheng, J. Tian, S. Wang, Y. Sun, K. Wang, F. Wang, Q. Zhang, Q. Meng, Y. Qi, Y. Yu, and X. Li, "In vivo study of retinal transmission function in different sections of the choroidal structure using multispectral imaging," *Invest. Ophthalmol. Visual Sci.* **56**(6), 3731–3742 (2015).
21. C. Zimmer, D. Kahn, R. Clayton, P. Dugel, and K. B. Freund, "Innovation in diagnostic retinal imaging: multispectral imaging," *Retin. Today* **9**(7), 94–99 (2014).
22. K. A. Firn, B. Khoobeji, and S. C. Ave, "Novel, noninvasive multispectral snapshot imaging system to measure and map the distribution of human retinal vessel and tissue hemoglobin oxygen saturation," *Int. J. Ophthalmic Res.* **1**(2), 48–58 (2015).
23. N. Lee, J. Wielaard, A. A. Fawzi, P. Sajda, A. F. Laine, G. Martin, M. S. Humayun, and R. T. Smith, "In vivo snapshot hyperspectral image analysis of age-related macular degeneration," in *2010 Annual International Conference of the IEEE Engineering in Medicine and Biology (EMBC)* (2010), pp. 5363–5366.
24. H. Li, W. Liu, B. Dong, J. V. Kaluzny, A. A. Fawzi, and H. F. Zhang, "Snapshot hyperspectral retinal imaging using compact spectral resolving detector array," *J. Biophotonics* **10**(6-7), 830–839 (2017).
25. F. M'hiri, C. Chevrefils, and J. P. Sylvestre, "Quality Assessment of Retinal Hyperspectral Images Using SURF and Intensity Features," in *20th International Conference on Medical Image Computing and Computer-Assisted Intervention (MICCAI)* (2017), pp. 118–125.
26. Z. Wang, M. Uemura, H. Takehara, M. Haruta, H. Tashiro, K. Sasagawa, and J. Ohta, "Near-infrared fundus camera with a patterned interference filter for the retinal scattering detection," *Jpn. J. Appl. Phys.* **60**(SB), SBBL07 (2021).
27. N. Pasychnikova, V. Naumenko, A. Korol, and O. Zadorozhnyy, "Digital imaging of the fundus with long-wave illumination," *Klinika Oczna* **111**(1-3), 18–20 (2009).
28. D. Toslak, T. Son, M. K. Erol, H. Kim, T. H. Kim, R. V. P. Chan, and X. Yao, "Portable ultra-widefield fundus camera for multispectral imaging of the retina and choroid," *Biomed. Opt. Express* **11**(11), 6281–6292 (2020).
29. T. Alterini, F. Díaz-Doutón, F. J. Burgos-Fernández, L. González, C. Mateo, and M. Vilaseca, "Fast visible and extended near-infrared multispectral fundus camera," *J. Biomed. Opt.* **24**(9), 096007 (2019).
30. D. Salo, D. Kim, Q. Cao, and M. Y. Berezin, "Multispectral imaging/deep tissue imaging: extended near-infrared: a new window on in vivo bioimaging," *BioOpt. World* **7**, 22–25 (2014).
31. T. Kubena, M. Kofronova, and P. Cernosek, "Nerve fiber layer defects imaging in glaucoma," in *The Mystery of Glaucoma* (InTechOpen, 2011), pp. 187–198.
32. M. Yanoff and J. W. Sassani, "Optic Nerve," in *Ocular Pathology* (Elsevier, 2015), pp. 441–465.
33. P. Campolmi, G. Cannarozzo, F. Dragoni, R. Conti, and S. Moretti, "Efficacy of rhodamine light in the treatment of superficial vascular lesions of the face," *Med. Prin. Pract.* **25**(5), 477–482 (2016).
34. C. D. Hanning and J. M. Alexander-Williams, "Pulse oximetry: A practical review," *Bmj* **311**(7001), 367–370 (1995).
35. M. Hammer, T. Riemer, W. Vilser, S. Gehlert, and D. Schweitzer, "A new imaging technique for retinal vessel oximetry: principles and first clinical results in patients with retinal arterial occlusion and diabetic retinopathy," *Proc. SPIE* **7163**, 71630P (2009).
36. I. Alabboud, D. Mordant, A. McNaught, and A. R. Harvey, "Quantitative spectral imaging of the retina," in *The Association for Research in Vision and Ophthalmology Annual Meeting (ARVO)* (2007).
37. J. G. Dwight, C. Y. Weng, R. E. Coffee, M. E. Pawlowski, and T. S. Tkaczyk, "Hyperspectral image mapping spectrometry for retinal oximetry measurements in four diseased eyes," *Int. Ophthalmol. Clin.* **56**(4), 25–38 (2016).
38. A. E. Elsner, S. A. Burns, J. J. Weiter, and F. C. Delori, "Infrared imaging of sub-retinal structures in the human ocular fundus," *Vision Res.* **36**(1), 191–205 (1996).

39. X. R. Huang, Y. Zhou, R. W. Knighton, W. Kong, and W. J. Feuer, "Wavelength-dependent change of retinal nerve fiber layer reflectance in glaucomatous retinas," *Invest. Ophthalmol. Visual Sci.* **53**(9), 5869–5876 (2012).
40. C. L. Shields, M. Furuta, E. L. Berman, J. D. Zahler, D. M. Hoberman, D. H. Dinh, A. Mashayekhi, and J. A. Shields, "Choroidal nevus transformation into melanoma: analysis of 2514 consecutive cases," *Arch. Ophthalmol.* **127**(8), 981–987 (2009).
41. C. L. Shields, A. Mashayekhi, M. A. Materin, C. K. Luo, B. P. Marr, H. Demirci, and J. A. Shields, "Optical coherence tomography of choroidal nevus in 120 patients," *Retina* **25**(3), 243–252 (2005).